

Near UV-Irradiation of CuOx-Impregnated TiO2 Providing Active Species for H2 Production Through Methanol Photoreforming

Original

Near UV-Irradiation of CuOx-Impregnated TiO2 Providing Active Species for H2 Production Through Methanol Photoreforming / Vitiello, G.; Clarizia, L.; Abdelraheem, W.; Esposito, S.; Bonelli, B.; Ditaranto, N.; Vergara, A.; Nadagouda, M.; Dionysiou, D. D.; Andreozzi, R.; Luciani, G.; Marotta, R.. - In: CHEMCATCHEM. - ISSN 1867-3880. - 11:17(2019), pp. 4314-4326. [10.1002/cctc.201900818]

Availability:

This version is available at: 11583/2767512 since: 2019-11-15T14:46:45Z

Publisher:

Wiley Blackwell

Published

DOI:10.1002/cctc.201900818

Terms of use:

This article is made available under terms and conditions as specified in the corresponding bibliographic description in the repository

Publisher copyright

(Article begins on next page)

Heterogeneous & Homogeneous & Bio- & Nano-

CHEMCATCHEM

CATALYSIS

Accepted Article

Title: Near UV-irradiation of CuOx-impregnated TiO2 providing active species for H2 production through methanol photoreforming

Authors: Giuseppina Luciani, Giuseppe Vitiello, Laura Clarizia, Wael Abdelraheem, Serena Esposito, Barbara Bonelli, Nicoletta Ditaranto, Alessandro Vergara, Mallikarjuna Nadagouda, Dionysios D. Dionysiou, Roberto Andreozzi, and Raffaele Marotta

This manuscript has been accepted after peer review and appears as an Accepted Article online prior to editing, proofing, and formal publication of the final Version of Record (VoR). This work is currently citable by using the Digital Object Identifier (DOI) given below. The VoR will be published online in Early View as soon as possible and may be different to this Accepted Article as a result of editing. Readers should obtain the VoR from the journal website shown below when it is published to ensure accuracy of information. The authors are responsible for the content of this Accepted Article.

To be cited as: *ChemCatChem* 10.1002/cctc.201900818

Link to VoR: <http://dx.doi.org/10.1002/cctc.201900818>

WILEY-VCH

www.chemcatchem.org



1 **Accepted Article**

2

3

4

5 **Near UV-irradiation of CuO_x-impregnated TiO₂ providing active**
6 **species for H₂ production through methanol photoreforming**

7

8 Giuseppe Vitiello^[a,b], Laura Clarizia^{*,[a]}, Wael Abdelraheem^[c,d], Serena Esposito^[e],
9 Barbara Bonelli^[f], Nicoletta Ditaranto^[g], Alessandro Vergara^[h], Mallikarjuna Nadagouda^[i],
10 Dionysios D. Dionysiou^[c], Roberto Andreozzi^[a], Giuseppina Luciani^{*,[a]}, Raffaele Marotta^[a]

11

12 [a] Department of Chemical, Materials and Production Engineering (DICMaPI), University of Naples
13 Federico II, p.le Tecchio 80, 80125 Naples, Italy.

14 [b] CSGI - Center for Colloids and Surface Science, via della Lastruccia 3, 50019 Sesto Fiorentino
15 (FI), Italy.

16 [c] Environmental Engineering and Science Program, Department of Chemical and Environmental
17 Engineering, 705 Engineering Research Center, University of Cincinnati, Cincinnati, OH 45221-
18 0012, United States.

19 [d] Department of Chemistry, Faculty of Science, Sohag University, 82524 Sohag, Egypt.

20 [e] Department of Civil and Mechanical Engineering, University of Cassino and South of Lazio, Via
21 G. Di Biasio 43, 03043 Cassino (FR), Italy.

22 [f] Department of Applied Science and Technology and INSTM Unit of Turin-Polytechnic,
23 Polytechnic of Turin, C.so Duca degli Abruzzi 24, I-10129 Turin, Italy.

24 [g] Department of Chemistry, University of Bari Aldo Moro, via Orabona 4, 70125 Bari, Italy.

25 [h] Department of Chemical Sciences, University of Naples Federico II, Complesso di Monte S.
26 Angelo, 80126 Naples, Italy.

27 [i] Department of Mechanical and Materials Engineering, Wright State University, Dayton, Ohio
28 45324, United States.

29 **Corresponding Authors:* Giuseppina Luciani (giuseppina.luciani@unina.it), Laura Clarizia
30 (laura.clarizia2@unina.it)

31

32

33

34 **Abstract**

35 Copper doped-TiO₂ (P25) nanomaterials have been intensively studied as promising catalysts for H₂
36 production by photo-reforming of selected organic compounds. However, the role of copper oxidation
37 states on the improvement of photocatalytic activity is still debated. In this work, CuO_x-impregnated
38 P25-TiO₂ catalysts were used for photocatalytic production of hydrogen from methanol. Copper
39 species/oxidation states both in the as-prepared catalysts and after the photocatalytic process were
40 investigated. To this purpose, H₂ production rates were correlated to physico-chemical properties of
41 the samples, both before and after photocatalytic process, by means of Raman, X-Ray Diffraction,
42 Electron Paramagnetic Resonance spectroscopy, X-Ray Photoelectron Spectroscopy, Temperature-
43 Programmed Reduction and High Resolution Transmission Electron Microscope techniques. Results
44 revealed the presence of both Cu₂O and CuO deposits on the samples surface after calcination.
45 Notably, under near-UV irradiation, the fraction of highly dispersed CuO particles undergo a partial
46 dissolution process, followed by reduction to metallic copper Cu_(s) by photogenerated electrons,
47 boosting H₂ production rate. Our findings indicate that both Cu₂O and Cu_(s) act as co-catalysts for H₂
48 generation, yet by different mechanisms. Overall this study, lies the basis to enhance catalytic
49 performance of red-ox active systems through UV-irradiation approach.

50

51 *Keywords:* copper-based TiO₂, hydrogen production, photoreforming, photocatalysis, methanol.

52

53 **Introduction**

54 Limited availability of fossil fuels as well as their environmental impact has prompted scientific
55 research towards cleaner and renewable energy sources. In this scenario, sunlight-driven H₂
56 production by either photo-reforming or water photo-splitting holds a great promise.^[1,2] However,
57 photoreforming-based technologies have been far from practical application and suffer from poor
58 efficiencies.^[1] Thus, improvement and optimization of photocatalytic systems are crucial tasks to
59 make this technology feasible.^[3] Indeed, photocatalysts with appropriate band-gap and adequate
60 stability for either organic photo-reforming or water-splitting under visible light irradiation with
61 suitable energy efficiencies are still unavailable, and their development is considered a significant
62 challenge in photocatalysis research.^[4,5]

63 Even though titanium dioxide in P25 form (80:20 w/w anatase:rutile) is considered one of the most
64 promising commercial material for photocatalytic processes, it shows significant limitations, such as
65 fast electron/hole recombination and absorption/activity restricted to the UV region due to its wide
66 bandgap.^[6,7] Among the various methods employed for improving TiO₂ properties, doping with noble
67 metals (Au, Pt, Pd) acting as co-catalysts has proven to be effective to enhance the photo-efficiency
68 of titanium dioxide.^[3,8-10]

69 Alternatively, doping with transition metal ions such as Cu, Fe, Co, Ni is a cheaper promising
70 option.^[6,9,11-13] The advantages of adopting these species lie in their behavior as electron scavengers,
71 thus limiting charge recombination.^[9, 10, 14-16] In particular, copper loaded-P25 nanomaterials,
72 prepared by impregnation method, have been proposed as promising catalysts for photo-reforming.^{[17-}
73 ^{19]} Although several studies have investigated the effect of copper loading on P25 nanoparticles for
74 the photocatalytic hydrogen generation through reforming of organics (Table 1), the effect of copper
75 oxidation state on the improvement in photocatalytic activity, is not yet entirely clarified. Different
76 conflicting opinions have been provided on synergistic effects of active copper species in photo-
77 catalytic reactions.

78

79 **Table 1** - Selected research papers devoted to testing Cu/P25 photocatalysts, prepared by
 80 impregnation method, in various photocatalytic processes.

Precursor	Calcination temperature (°C)	Cu oxidation state	Diagnostic technique	Application	Ref.
$\text{Cu}(\text{NO}_3)_2 \times 3\text{H}_2\text{O}$	300 – 500 for 0.5 h	CuO	TPR, XRD	Hydrogen production	[20]
$\text{Cu}(\text{NO}_3)_2 \times 2.5\text{H}_2\text{O}$	300 for 5 h (in air)	CuO	TPR	CO oxidation	[21]
$\text{Cu}(\text{NO}_3)_2 \times 2.5\text{H}_2\text{O}$	300 for 5 h (in air)	CuO/Cu ₂ O	TPR, XRD, XPS, Raman	CO oxidation	[22]
$\text{Cu}(\text{NO}_3)_2$	400 for 16 h (in air)	CuO	TPR, XRD, FTIR	Hydrogenation of 1,3-cyclooctadiene	[23]
$\text{Cu}(\text{CH}_3\text{COO})_2 \times \text{H}_2\text{O}$	250 for 4 h (in air)	Cu ²⁺ /Cu ⁺	TPR, XPS, FTIR	Hydrogenation of crotonaldehyde	[24]
$\text{Cu}(\text{NO}_3)_2$	400 for 1h (in Helium)	CuO/Cu ₂ O	TPR, XPS, FTIR,	CO oxidation	[25]
$\text{Cu}(\text{NO}_3)_2$	300 – 500 for 5 h	CuO/Cu ₂ O	DRS, XPS, FTIR	Hydrogen production	[26]
$\text{Cu}(\text{NO}_3)_2 \times 3\text{H}_2\text{O}$	300 for 0.5 h (in air)	CuO/Cu ₂ O	XPS, XRD	Hydrogen production	[27]
$\text{Cu}(\text{CH}_3\text{COO})_2 \times \text{H}_2\text{O}$ or $\text{Cu}(\text{NO}_3)_2$	500 – 600 for 1 h (in Argon)	CuO/Cu ₂ O	XRF, XRD	Acetic acid decomposition, hydrogen production	[28]
$\text{Cu}(\text{NO}_3)_2 \times 3\text{H}_2\text{O}$	400 for 2 h	CuO	XANES, EXAFS	Methylene blue degradation	[29]
$\text{Cu}(\text{NO}_3)_2$	350 for 4 h (in air)	CuO	XRD	Hydrogen production	[30]
$\text{Cu}(\text{NO}_3)_2 \times 3\text{H}_2\text{O}$	350 for 2 h (in air)	Cu ₂ O	XPS, XRD	Hydrogen production	[31]

$\text{Cu}(\text{NO}_3)_2$	100 – 600 n.r.	CuO	XPS, XRD	Hydrogen production	[32]
$\text{Cu}(\text{NO}_3)_2$	350 for 4 h (in air)	CuO	XRD	Hydrogen production	[33]
$\text{Cu}(\text{NO}_3)_2 \times 3\text{H}_2\text{O}$	450 for 4 h (in air)	CuO	XPS, XRD	Hydrogen production	[34]
$\text{Cu}(\text{NO}_3)_2 \times 3\text{H}_2\text{O}$	450 for 4 h (in air)	CuO , $\text{Cu}_x\text{Ti}_{1-x}\text{O}_2$	XRD, XANES, EXAFS	Hydrogen production	[35]
CuCO_2CH_3	400 for 1h (in air)	Cu_2O , CuO	XPS, XRD, DRUV	Gallic Acid degradation	[36]

81

82 Several studies report that Cu_2O species are responsible for enhanced photocatalytic H_2 production
83 from water.^[8,9,25,37] On the other hand, the presence of CuO was argued by different authors to be
84 responsible for the enhanced separation of photoinduced electrons and holes.^[3,30,32,33] Similarly,
85 Valero et al. proposed that easily reduced Cu^{2+} species could be responsible for higher Cu/P25
86 photoactivity.^[38] Other scientific studies also ascribe the improved photocatalytic activity of Cu/P25
87 systems to the presence of finely dispersed and easily reducible CuO_x (Cu^+/Cu) species on the TiO_2
88 surface.^[39] Such widespread variability in scientific conclusions is due to an intrinsic complexity of
89 materials during photocatalytic experiments, along with different impregnation procedures for copper
90 doping of P25 resulting in mixed oxidation states of copper on the catalyst surface. Typically, copper
91 exists in different oxidation states ($\text{Cu}_{(s)}$, Cu^+ , Cu^{2+}), that can change under UV-irradiation.^[40-42]
92 In this scenario, the present paper aims at elucidating the nature of copper species in Cu/ TiO_2
93 photocatalysts prepared via impregnation-calcination method. Moreover, evolution of copper species
94 under UV-irradiation during phot-reforming process was investigated, in order to clearly identify the
95 active species involved in H_2 production. Hydrogen production rates were compared and integrated
96 with a detailed physico-chemical characterization of the catalyst before and after the photo-catalytic

5

97 process, through a combined approach of complementary techniques, including X-Ray diffraction
98 (XRD), X-Ray Photoelectron Spectroscopy (XPS), Raman and Electron Paramagnetic Resonance
99 (EPR) Spectroscopies, Scanning Electron Microscopy (SEM), High Resolution Transmission
100 Electron Microscopy (HR-TEM), and Temperature Programmed Reduction (TPR) analysis. This
101 study is expected to deliver significant insights on the molecular factors responsible for the improved
102 photocatalytic activity of Cu-based TiO₂ materials, thus providing critical guidelines for the design
103 of new copper doped photocatalysts for UV-solar photoreforming.

104

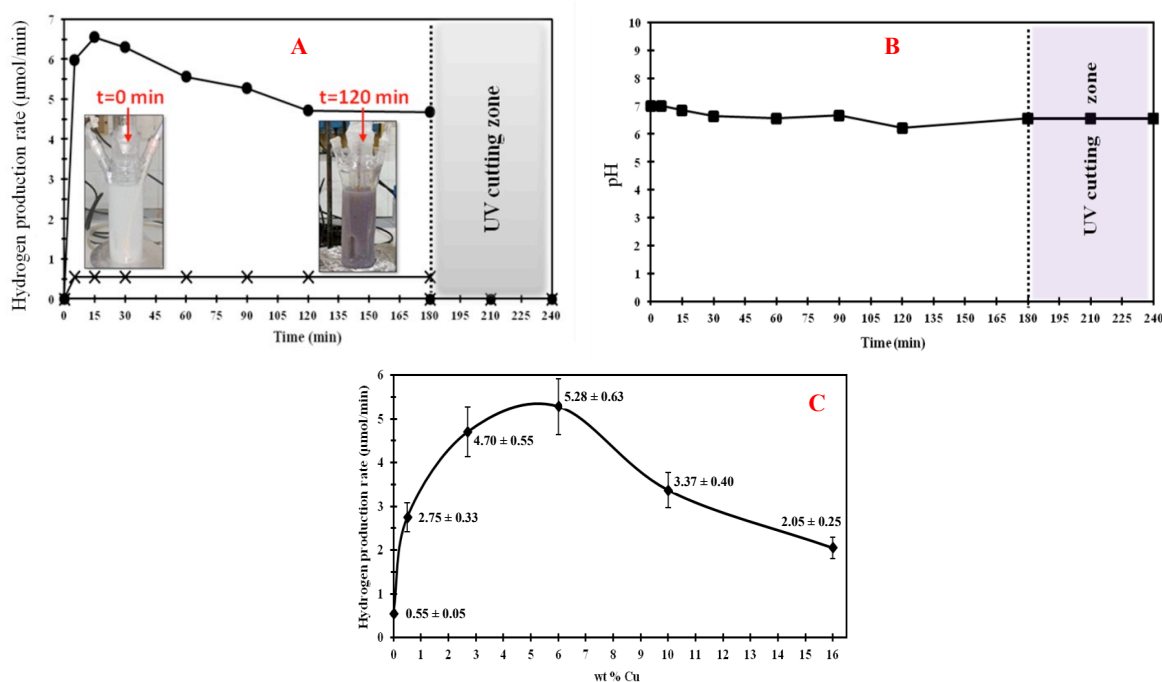
105 **Results and Discussion**

106 **Photocatalytic tests**

107 *Effect of photocatalyst copper content on H₂ generation*

108 P25-based samples with different copper weight percentages, in the range 0.5-16 wt%, were tested
109 for hydrogen generation through photoreforming of methanol. Figure 1A shows H₂ production rate
110 of Cu(3%)/P25 after calcination at 350 °C; this trend, approaching a plateau within about 120 minutes,
111 is representative of all compositions. During the photocatalytic run, the suspension turned from light
112 teal to deep indigo, thus suggesting that a change in copper oxidation state occurred under UVA
113 irradiation.^[27] After 180 minutes of reaction, UVA radiation was cut off by inserting a NaNO₂ solution
114 (1 M) into the cooling system, as previously proposed and described in the Experimental section.^[43]
115 Such procedure allowed to test the photocatalytic activity under only visible light irradiation. No
116 hydrogen generation was recorded for any catalysts tested under only visible light irradiation, thus
117 indicating that such system are activated by UV irradiation. Furthermore, hydrogen production rates
118 were remarkably higher than values obtained over bare P25-TiO₂ calcined under inert atmosphere at
119 350 °C for 5 hours (0.55 μmol/min) and comparable to the values measured by Jung et al. by using
120 H₂-treated Cu/P25 samples.^[27] Figure 1B depicts the change in solution pH during the photoreforming
121 run. There was no changes in pH, which kept constant at about 6.5 throughout the experiment.
122 Furthermore, no trace of dissolved copper was detected throughout the experiment, thus suggesting

123 a high stability of the photocatalyst. Figure 1C shows hydrogen production rate as a function of copper
 124 content. A non-monotonic trend was observed, with catalysts containing 3% and 6% weight
 125 percentages of copper displaying comparable similar values of hydrogen production rate, which were
 126 also the highest recorded. All Cu/P25 systems showed higher light absorption capability than bare
 127 P25-TiO₂ both in the UV and visible range (Figure S1A-B), although this did not result in a catalytic
 128 activity of the Cu-doped catalyst under visible light irradiation.



129 **Figure 1. Panel A:** Hydrogen production rate over (●) Cu(3%)/P25 and (×) bare P25-TiO₂, both
 130 calcined under inert atmosphere at 350 °C for 5 hours. After 180 minutes of reaction, UVA radiation
 131 has been cut off by inserting 1 M NaNO₂ solution into the cooling system. Catalysts load =150 mg/L.
 132 [CH₃OH]₀ = 2.47 M. T=25 °C. P=1atm. The insets represent the colour suspension with Cu(3%)/P25
 133 before and after 120 min of reaction. **Panel B:** Solution pH throughout the photoreforming run over
 134 Cu(3%)/P25 catalyst calcined under inert atmosphere at 350 °C for 5 hours. After 180 minutes of
 135 reaction, UVA radiation was cut off by inserting 1M NaNO₂ solution into the cooling system.
 136 Cu(3%)/P25 catalyst load=150 mg/L. [CH₃OH]₀ = 2.47 M. T=25 °C. P=1 atm). For each value, 12%
 137 error was considered, based on the results of a reproducibility photoreforming run performed over
 138 Cu(3%)/P25 calcined at 350 °C. **Panel C:** Plateau values of hydrogen production rate recorded over
 139 P25-TiO₂ catalysts calcined under inert atmosphere at 350 °C for 5 hours with different copper
 140 content. Weight percentages of copper: 0.5%, 3%, 6%, 10%, 16%. Cu/P25-TiO₂ catalysts load=150
 141 mg/L. [CH₃OH]₀ = 2.47 M. T=25 °C. P=1 atm.

142
 143
 144
 145 *Effect of photocatalyst calcination temperature on H₂ generation*

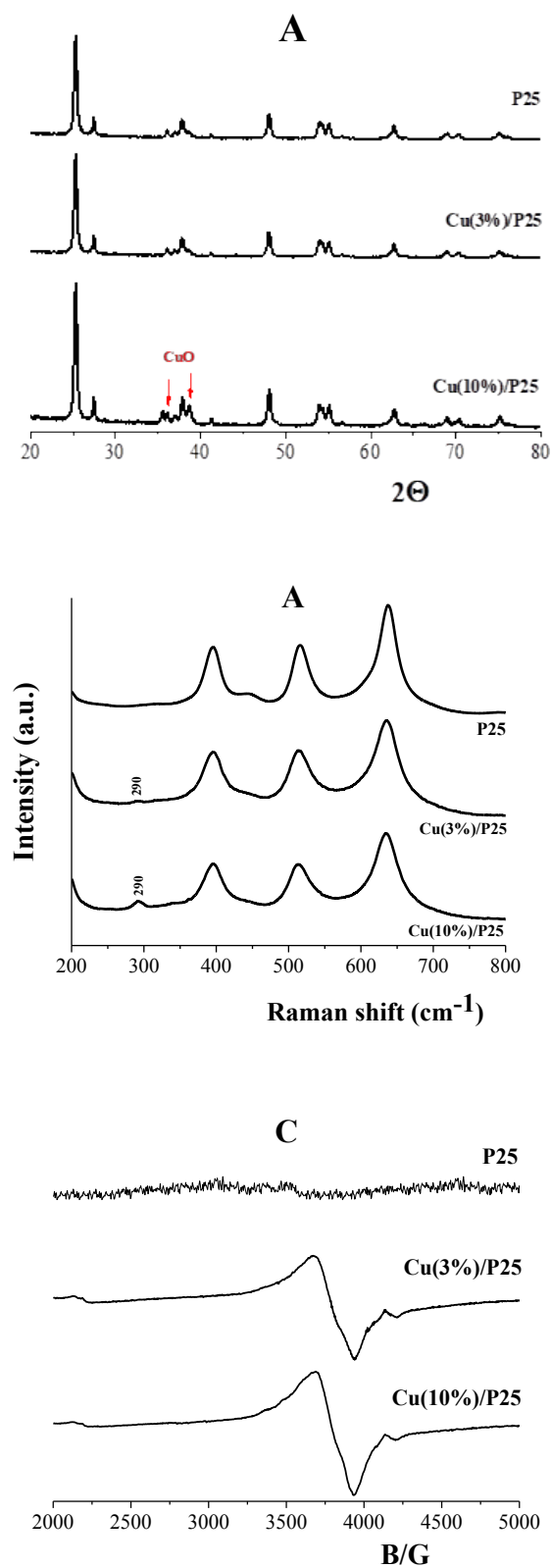
146 Cu/P25 samples calcined under inert N₂ atmosphere for 5 hours at different temperatures were tested
 147 for hydrogen generation through photo-reforming of methanol. Calcination temperatures were

148 investigated in the range of 150-550 °C (Figure S2, Supplementary Information). Similar values of
149 hydrogen generation rates were achieved by using catalysts calcined at 150-350 °C, though, further
150 increase in calcination temperature showed detrimental results in terms of photoefficiency for
151 hydrogen generation. Once again, no hydrogen evolution was recorded by excluding UV irradiation
152 for all catalysts tested.

153 **Characterization of the fresh photocatalysts**

154 Detailed physico-chemical characterizations of Cu/P25 samples were carried, before and after
155 photocatalytic experiments, in order to investigate changes in catalysts' properties upon use for H₂
156 production under near-UV irradiation. In particular, copper oxidation states in Cu deposited species
157 on P25 surface were assessed both before and after photocatalytic experiment with the aim of
158 revealing their role in the enhancement of photocatalytic H₂ production. The measured values of BET
159 surface specific area (S_{BET}) for Cu/P25 catalysts calcined at different temperatures or with different
160 Cu loads are summarised in Table S1 (Supplementary Information). No particular changes were
161 observed before and after use (data not shown), but a significant decrease in the surface area was
162 recorded for the catalyst calcined at 550 °C, likely due to some aggregation phenomenon.
163 Specifically, the highest surface area of 41 m²/g was recorded for Cu(3%)/P25 calcined at 350 °C.
164 XRD spectra were collected in order to assess crystalline properties in the catalysts. Figure 2A shows
165 XRD spectra of bare P25, fresh Cu(3%)/P25 and Cu(10%)/P25 calcined at 350 °C for 5h. Peaks of
166 anatase and rutile structures appeared in all samples. Furthermore, XRD profiles of the fresh
167 Cu(3%)/P25 samples did not show any diffraction peaks of CuO_x species, in agreement with the low
168 amount of Cu. On the contrary, XRD spectrum of Cu(10%)/P25 sample highlighted two diffraction
169 peaks at about 36.5° and 38.5°, displaying the presence of CuO.^[27] Comparison of the peak intensities
170 of rutile and anatase revealed the typical composition of P25 samples that was not altered neither by
171 Cu impregnation (Figure 2A). Furthermore, no relevant changes in peak position and intensity were

172 appreciated the XRD patterns of samples treated up to 450 °C (Figure S3), revealing that thermal
173 treatment did not significantly alter the samples crystalline structure.

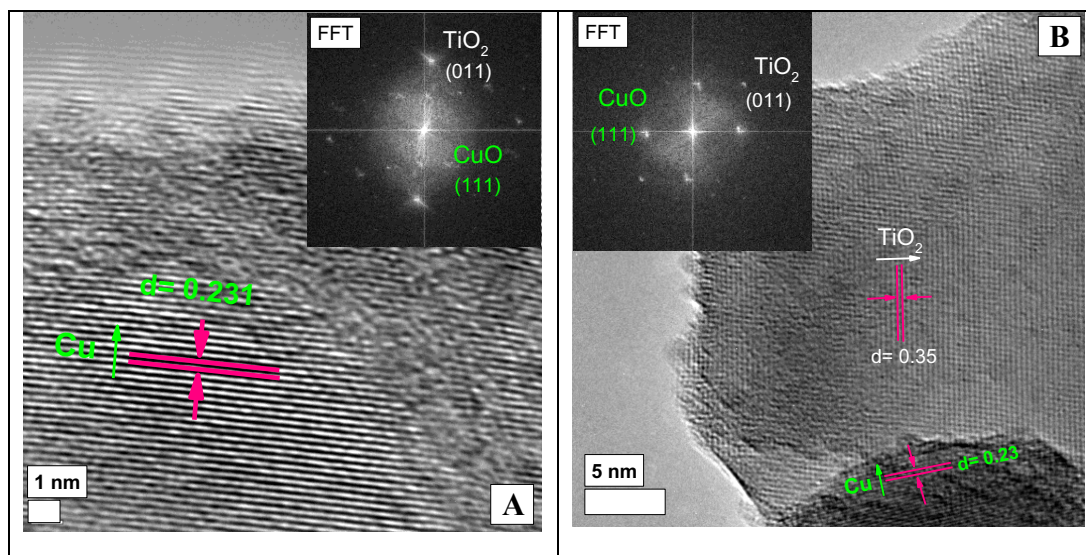


174

175 **Figure 2.** XRD patterns (**panel A**), Raman spectra (**panel B**) and normalized EPR spectra (**panel C**)
176 of bare P25, fresh Cu(3%)/P25 and Cu(10%)/P25 calcined at 350 °C for 5h.

177 Raman and EPR spectra were also recorded in order to define the oxidation state of copper
178 impregnated on the P25 surface for materials before their use (Figure 2B-C). Concerning the fresh
179 Cu/P25 catalyst, Raman spectra were recorded on Cu(3%)/P25 and Cu(10%)/P25 samples (Figure
180 2B) also compared to P25 as reference material. Both catalysts showed a peak at 290 cm^{-1} , which is
181 ascribable to the Raman band of CuO. Although it is usually detected around 279 cm^{-1} , and is
182 associated to an A_g mode,^[45] the upshift in wavenumbers observed in our experiments compared to
183 pure CuO can occur either due different structuring or to interactions with the hosting matrix (herein
184 TiO_2). On the other hand, the typical most intense Raman band of Cu_2O and corresponding to the
185 second order overtone $2\Gamma_{12^-}$ (216 cm^{-1})^[44] was never visible in any analysed catalyst (Figure 2B). The
186 presence of cupric species in pre-used (fresh) Cu(3%)/P25 and Cu(10%)/P25 catalysts was also
187 confirmed by EPR spectra (Figure 2C) showing an asymmetric signal for both samples at a g-factor
188 of ~ 2.0800 , which is larger than the g-value of free electron $g_e = 2.0023$ and is related to the presence
189 of Cu^{2+} in the distorted octahedral coordination of TiO_2 .^[46] The broadness of the EPR spectra indicates
190 the presence of dipolar interaction among neighboring Cu^{2+} ions that leads to the increase in the width
191 of the EPR signal.

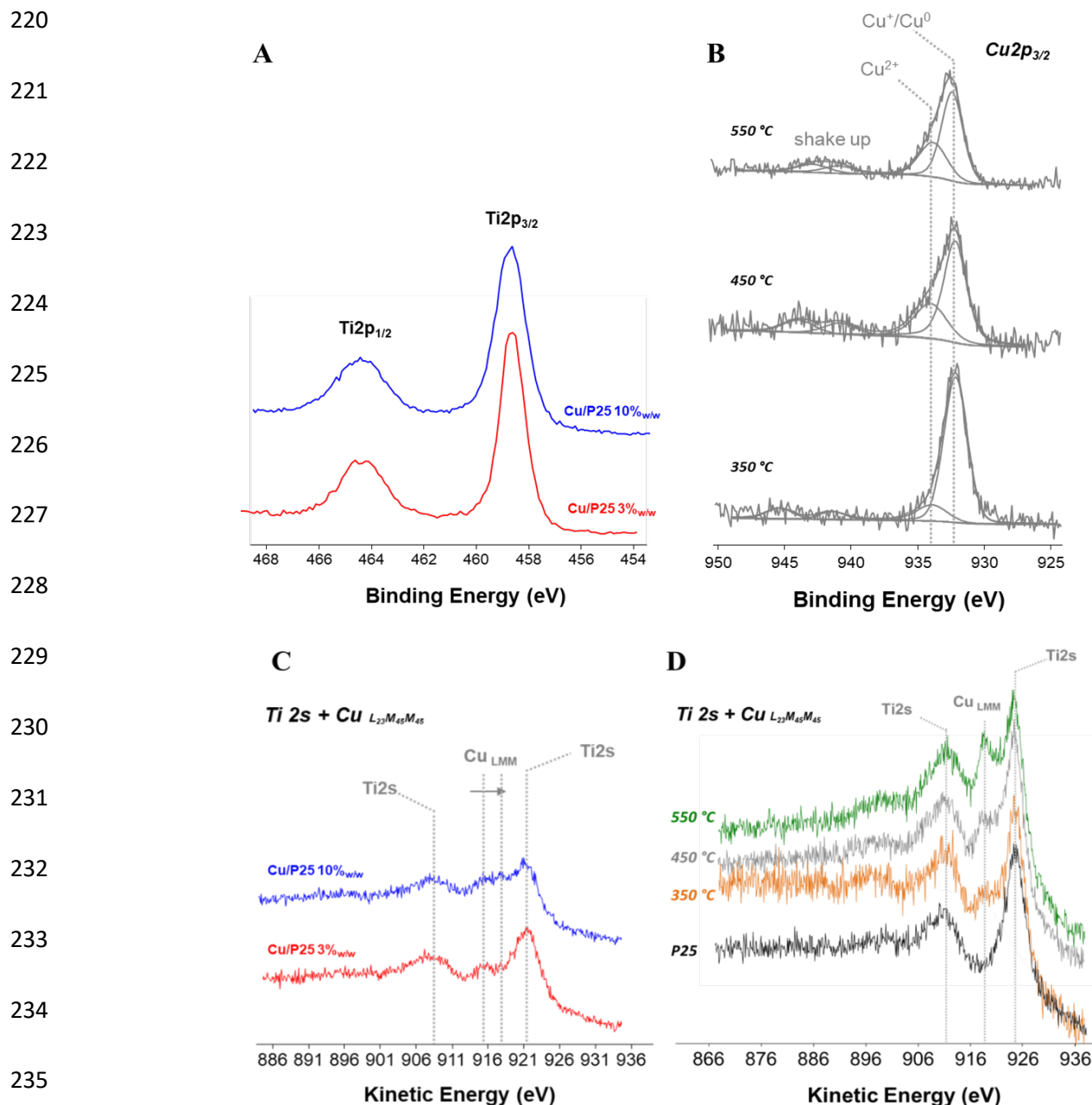
192 Therefore, XRD, EPR and Raman analyses confirm the presence of CuO in Cu/P25 samples.
193 Morphology, crystal structure and copper oxidation states were also assessed through TEM analyses.
194 Figure 3A shows HR-TEM and Fast Fourier Transform (FFT) analyses for fresh Cu(3%)/P25 sample
195 calcined at $350\text{ }^\circ\text{C}$. An interplane distance of $d_{\text{Cu}} = 0.231\text{ nm}$ calculated from the HR-TEM micrograph
196 (Figure 3A), corresponding to the (111) plane of CuO, further confirmed its presence on TiO_2 (d_{TiO_2}
197 $= 0.33\text{ nm}$), in accordance with XRD, Raman and EPR results. Moreover, FFT image (*inset* of Figure
198 3C) clearly justified the existence of TiO_2 material in amorphous structure with some clear spots
199 related to the co-existed CuO particles.



200

201 **Figure 3.** HR-TEM for fresh Cu(3%)/P25 sample calcined at 350 °C (**A**, inset: FFT analysis) and for
 202 fresh Cu(10%)/P25 catalyst calcined at 350 °C (**B**, inset: FFT analysis).
 203

204 Changing Cu composition in Cu/P25 catalyst to 10% while maintaining the calcination temperature
 205 at 350 °C did not lead to a significant alteration in the catalyst structure (Figure 3B), however larger
 206 surface deposits were appreciated (Figure 3B). To further clarify the oxidation state of surface Cu-
 207 species, samples were analyzed by means of XPS analysis. Higher temperatures led to an increase of
 208 copper surface availability, as evident from Cu/Ti atomic ratio in Cu(3%)/P25 samples (Table S2).
 209 At 550 °C aggregation phenomena of copper particles can occur, resulting in higher Cu detected
 210 amount in the same analyzed spot. A similar trend is shown when the catalysts were prepared with
 211 increasing bulk copper loading, even at the lowest calcination temperature (Table S3). Actually, both
 212 the total copper increase and the eventual surface aggregation phenomena could contribute to the
 213 increase of copper amount detected on the surface. Indeed, the observed increase in Cu surface
 214 availability was not proportional to the overall Cu content; actual difference between them got wider
 215 with increasing copper loading, suggesting a different size distribution of copper species on TiO₂
 216 surface. Apart from total surface copper availability, XPS measurements were aimed at elucidating
 217 Cu and Ti oxidation state of Ti on TiO₂ surface. Figure 4A shows Ti2p XP spectral region of fresh
 218 Cu(3%)/P25 and Cu(10%)/P25 catalysts. XPS spectra of all catalysts with different copper loadings
 219 are reported in Figure S5.



236 **Figure 4.** Ti2p XP spectra of the fresh Cu(3%)/P25 and Cu(10%)/P25 catalysts calcined at 350 °C
 237 (A). Cu2p_{3/2} XP spectra of the fresh Cu(3%)/P25 sample at different calcination temperatures (B).
 238 Ti2s XP+Cu_{LMM} XAE spectra of Cu(3%)/P25 and Cu(10%)/P25 calcined at 350 °C (C) and of
 239 Cu(3%)/P25 at different calcination temperatures (D).

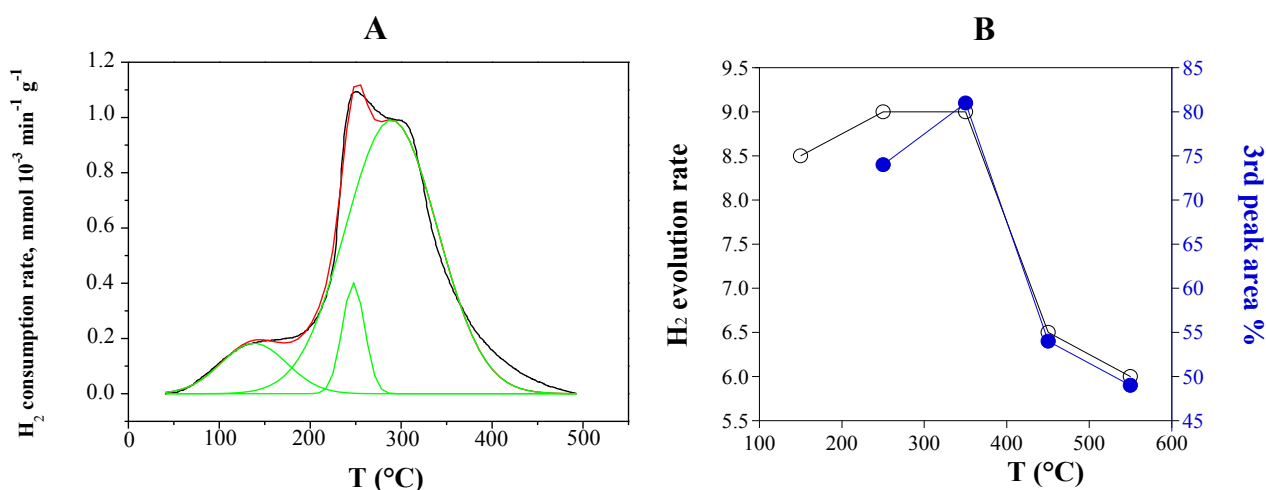
240

241 In all the spectra, the characteristic peaks of Ti2p_{3/2} and Ti2p_{1/2} were observed at BE values of
 242 458.7±0.1 eV and 464.4±0.1 eV, respectively, and were assigned to Ti⁴⁺ in TiO₂.^[1] A possible
 243 interaction between Cu species and P25 would result not only in the BE shift but also in the change
 244 of the spin-orbit splitting value in the Ti2p signal.^[1] Nevertheless, no significant variation was

245 observed neither changing the copper loading nor increasing the calcination temperature (Figure 4A,
246 Figure S5 in Supplementary Information); the value was measured to be constant and equal to 5.7
247 eV, therefore no Cu incorporation into the TiO₂ lattice could be hypothesized.^[2] Figure 4B reports
248 Cu2p_{3/2} XP spectra of the Cu(3%)/P25 catalyst calcined at different calcination temperatures. After
249 curve-fitting procedures, the main peak was identified at BE=932.4±0.1 eV in all the cases and was
250 ascribed to Cu⁺/Cu⁰ species.^[1,3] Furthermore, shake up satellites were visible (940-945 eV) along with
251 a peak at 934.0±0.1 eV, that was assigned to Cu²⁺ species.^[1,3] The copper spectral regions of the
252 catalysts prepared at higher bulk copper loadings (Figure 4A, Figure S5) as well as at different
253 calcination temperatures (Figure 4B) showed similar results. Particularly, for Cu(3%)/P25 sample at
254 different temperatures, a main peak due to Cu⁺/Cu⁰ species along with variable amounts of Cu²⁺,
255 depending on the Cu loading, was detected (Figure 4B). Since the binding energies of Cu⁺ and Cu⁰
256 are not distinguishable based on Cu2p_{3/2} XP peak, the spectral region relative to X-ray excited Auger
257 copper spectra (XAES Cu_{LMM}) were investigated to fully elucidate the oxidation state of the reduced
258 copper species. Figure 4 reports Cu_{LMM} spectra for fresh Cu(3%)/P25 and Cu(10%)/P25 samples
259 treated at 350 °C (C) and 3%Cu bulk loading at different calcination temperatures (D) .

260 A further challenge in the Cu⁺/Cu⁰ discrimination was represented from the partial overlapping of
261 Cu_{LMM} and the predominant Ti2s spectral regions (black line in Figure 4D). Nevertheless, the main
262 peak for copper was still detectable in all the samples and was found at KE=916.3±0.3 eV. Moreover,
263 the Auger parameter – the sum of the binding energy from XPS and the kinetic energy from XAES –
264 was calculated to be 1848.7±0.1 eV. Both the values demonstrated that the Cu⁺/Cu⁰ peak is ascribable
265 to Cu⁺ species.^[3] However, the absence of Cu⁰ traces could not be completely ruled out under these
266 experimental conditions, since the peak would fall at KE=918.6 ±0.2 eV, overlapped with Ti2s
267 peak.^[46] Similar results were obtained for XPS spectra of the samples at different calcination
268 temperatures (Figure 4D). When the relative abundance of Cu²⁺ is increased, the peak is shifted to
269 slightly higher KE values, according to KE values for oxidized copper species (Figure 4C).^[3]

270 To get a greater insight into the Cu-TiO₂ interaction as function of the annealing temperature, the
 271 reducibility of the samples was studied by means of the TPR technique. The TPR profile of
 272 Cu(3%)/P25 sample after calcination at 350 °C is shown in Figure 5A, while the TPR profiles of
 273 Cu(3%)/P25 sample after calcination at 250, 450 and 550 °C are reported in Figure S6
 274 (Supplementary Information). All of them are reported in the temperature range characteristic of
 275 copper oxide reduction,^[22,38,52] where instead TiO₂ reduction was hardly observed.



276 **Figure 5. Panel A:** TPR profile of Cu(3%)/P25 sample calcined at 350 °C. **Panel B:** H₂ evolution
 277 rate (○) and percentage of TPR 3rd peak area (●) as a function of calcination temperature for
 278 Cu(3%)/P25 sample.
 279

280

281 As indicated by the curve fit analysis, the samples showed a distribution of copper species;
 282 conversely, the unsupported CuO showed a single peak at 400 °C.^[45,46] The hydrogen consumption
 283 relative to each fitting peak for Cu(3%)/P25 is listed in Table 2 and Table S4 along with T_{max} values.
 284

284

285 **Table 2** - Results of TPR measurements for fresh Cu(3%)/P25 sample calcined at 350 °C

Sample	T _{max} (°C)	Hydrogen consumption (μmol/g)
Cu(3%)/P25	138, 246, 290	101, 76, 759

286

287 The assignment of the reduction peak at lower temperature is quite controversial: it is generally
 288 ascribed to the reduction of highly reducible Cu²⁺ species, though the presence of Cu⁺ species cannot

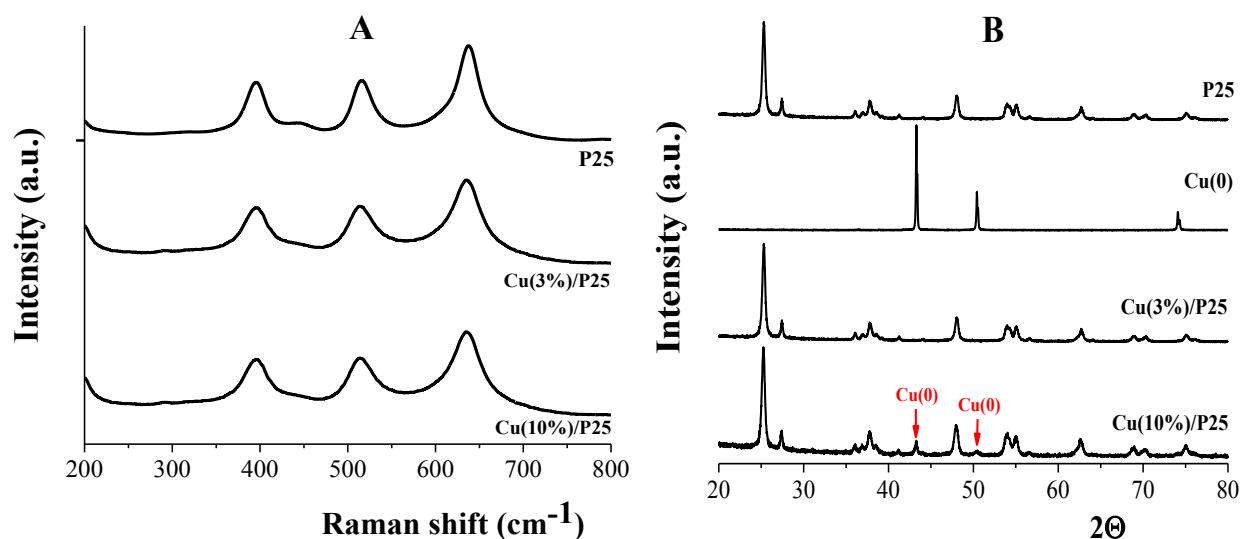
289 be ruled out.^[38] Indeed, Chen et al. ^[22] assigned the TPR peak in this range to the reduction of Cu⁺
290 species in Cu(3%)/P25 sample. The formation of Cu⁺ species was ascribed to the presence of oxygen-
291 defect vacancies in the TiO₂ structure. The presence of isolated Cu⁺ species and small Cu₂O cluster
292 with reduction peak at 157 °C and 208 °C, respectively was also proposed by Minsu Jung et al.^[52,53]
293 Samples treated at 250 °C and 350 °C, *i.e.* Cu(3%)/P25_250 and Cu(3%)/P25_350, showed the
294 highest hydrogen consumption in correspondence of the peak at about 280-290 °C associable to small
295 and/or highly dispersed CuO particles. TPR profile gradually changed by increasing the calcination
296 temperature, leading to a decrease of the peak at 280-290 °C and to the occurrence of another
297 reduction peak at higher temperature. Peaks located in the 320-400 °C temperature range are
298 indicative of the formation of bulky CuO species.^[45,46] Thus, it can be inferred that a lower calcination
299 temperature resulted in a better dispersion of copper species on the support. As far as the overall H₂
300 consumption is concerned, it was much higher with respect to the stoichiometric amount as calculated
301 under the hypothesis of the occurrence of all Cu as Cu²⁺ species. This likely indicated some spillover
302 phenomena of H₂ occurring over the support with the likely partial reduction of the latter, as generally
303 observed for copper doped anatase.^[54]

304 The influence of calcination temperature on hydrogen production rate is reported in Figure 5B,
305 together with the percentage of amount of the third peak area in TPR analysis. Actually, evolved H₂
306 amount appeared closely related to the fraction of highly dispersed CuO particles strongly interacting
307 with the support, probably accounting for the third peak area in TPR analysis (Table 2 and Table S4).

308 **Characterization of the used Cu/P25 photocatalysts**

309 The Cu/P25 catalysts were also analyzed after their use to assess any evolution of Cu oxidative state
310 during photocatalytic runs, so as to identify the nature of Cu-active species towards H₂ evolution as
311 well as their role in photocatalytic. Particularly, this investigation was carried out on both
312 Cu(3%)/P25 and Cu(10%)/P25 samples, calcined at 350 °C. Specifically, Raman spectra of both
313 samples after photocatalytic run, reported in Figure 6A, indicated that no peak ascribable to the

314 presence of cupric species was observed. This result was also confirmed by the EPR evidence
 315 indicating that these considered samples did not show any paramagnetic signal. Since no significant
 316 release of cupric ions was observed during photoreforming tests, obtained results suggest the
 317 reduction of the copper during the photoreforming process. Actually, the indigo color of the final
 318 suspension supported a change of the oxidation state of copper deposited on titania, further confirmed
 319 by XRD diffraction analysis too. Notably, XRD patterns of used Cu(10%)/P25 collected after the
 320 photocatalytic run, no longer showed diffraction peaks of CuO phase and clearly indicated the
 321 presence of Cu(0) diffraction peaks (Figure 6B). Unfortunately, due to the low Cu content, this peak
 322 was not detectable in the XRD spectrum of the used Cu(3%)/P25 sample.



323

324 **Figure 6. Panel A:** Raman spectra of bare P25, used Cu(3%)/P25 and Cu(10%)/P25 samples calcined
 325 at 350 °C for 5h. **Panel B:** XRD patterns of bare P25, Cu(0), used Cu(3%)/P25 and Cu(10%)/P25
 326 calcined at 350 °C for 5h.

327

328 HR-TEM and FFT analyses were performed on used Cu(3%)/P25 catalyst calcined at 350 °C, showing
 329 co-existence of Cu₂O and Cu⁰ on the TiO₂ particles, thus indicating CuO reduction (Figures 7) during
 330 the photocatalytic experiment. It is noteworthy mentioning the co-existence of Cu₂O and Cu⁰ in the
 331 used Cu/P25 catalysts was deduced from the indicated phase (111) that corresponds to both Cu₂O and
 332 Cu⁰,^[55] the latter also confirmed by XRD analysis. Again, Cu₂O (111) and Cu⁰ (111) were the
 333 dominant copper species in the 10%Cu-containing catalyst (Figure S7).

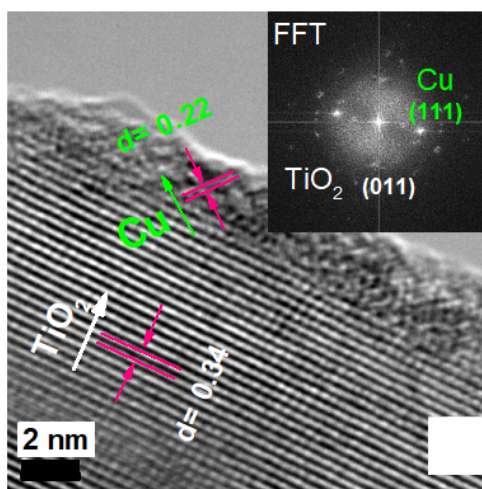


Figure 7. HR-TEM for used Cu(3%)/P25 sample calcined at 350 °C.

334

335

336

337 The comparison of XPS copper spectra of Cu(3%)/P25 before and after use are reported in Figure 8
 338 while Cu/Ti ratio for the same samples are reported in Table S5 (Supplementary Information).

339

340

341

342

343

344

345

346

347

348

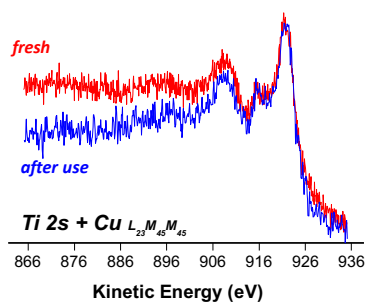
349

350

351

352

353



after use

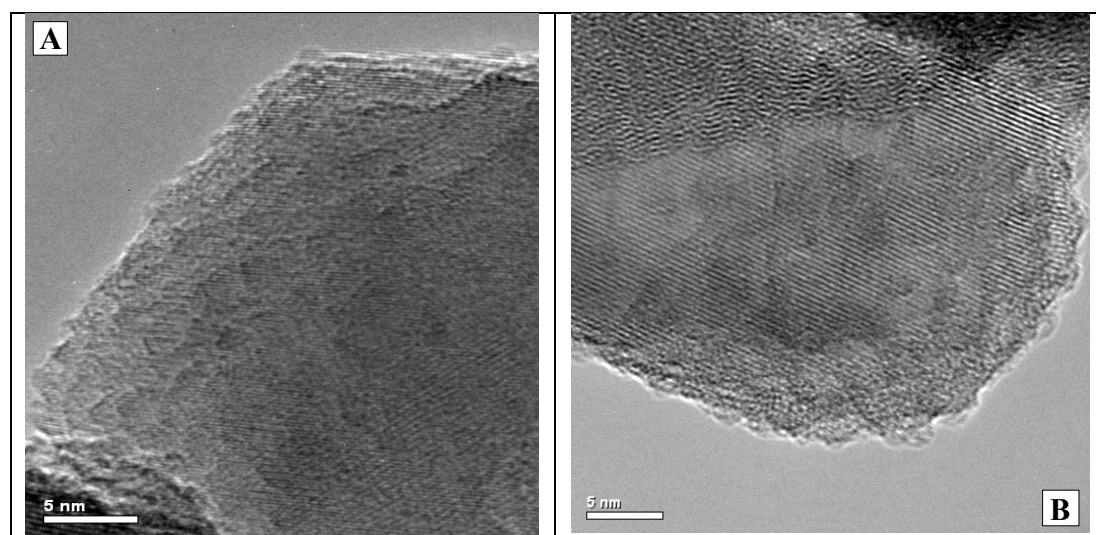
354
355
356
357
358
359
360
361
362
363
364
365
366
367
368
369

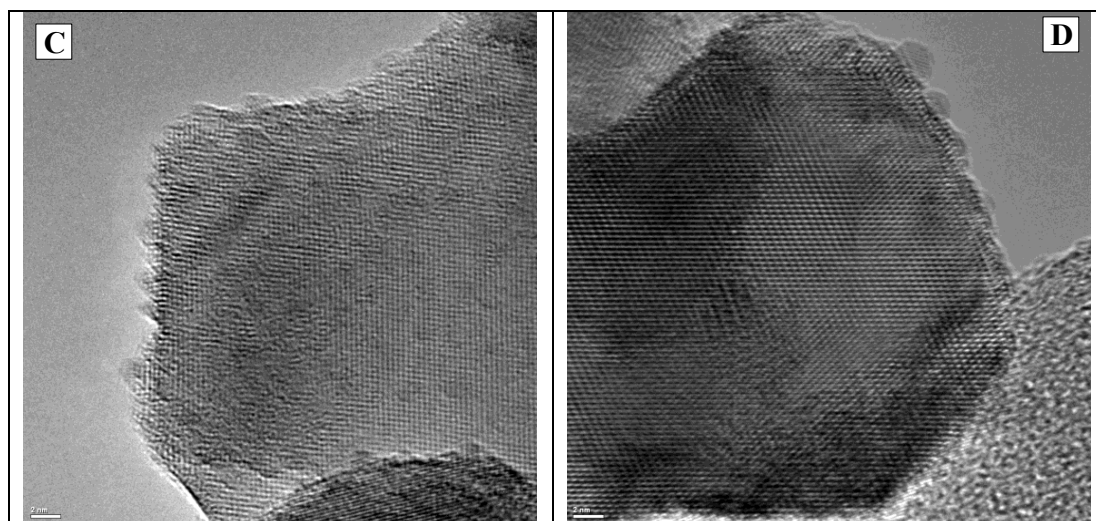
370 **Figure 8.** Cu_{2p_{3/2}} XP spectra for Cu(3%)/P25_350°C fresh and after use. Corresponding Cu_{LMM} XAE
371 spectra in the inset.

372 From XPS and XAES results no specific differences could be derived on the surface of the catalyst
373 before and after use. Both spectra presented a small amount of Cu²⁺ (peak at BE=, 934.0±0.1 eV,
374 along with shake up features) and the predominant Cu⁺/Cu⁰ oxidation state on the catalyst's surface
375 (main peak at BE=932.4±0.1 eV). Moreover, XAES peaks are completely overlapped. Furthermore,
376 Cu⁰ peak, if any, is overlapped with Ti_{2s} peak in XAE spectrum: this makes any possible change in
377 Cu⁰ amount hardly appreciable in the studied systems.^[49] Finally, Cu/Ti ratio slightly increased after
378 use (Table S5), probably due a different distribution of surface copper species.

379 Despite Cu-doped TiO₂ catalysts have been intensively studied for H₂ production through photo-
380 reforming, published results are still controversial on the activity of different Cu oxidation states.^{[20,26-}

381 ^{34]} Our results clearly showed that calcination of $\text{Cu}(\text{NO}_3)_2 \times 3\text{H}_2\text{O}$ -impregnated P25 samples under
382 nitrogen atmosphere leads to a mixture of CuO and Cu_2O nanostructures on P25 surface. The former
383 was clearly evidenced by bulk characterization techniques, in particular EPR and Raman
384 spectroscopy. Furthermore, XPS analysis proved the presence of surface Cu_2O as the predominant
385 CuO_x species. The poor CuO amount measured through this methodology, can be explained
386 considering this technique revealing composition of the more exposed layer on the surface. These
387 results supported earlier reports, where both oxidation states are observed for copper.^[22,24-28,36]
388 Furthermore, as a major point, from TPR analysis different populations of CuO_x species could be
389 distinguished on the catalysts. A highly dispersed fraction of small and dispersed CuO particles
390 strongly interacting with the support was appreciated on the catalysts with the highest H_2 evolution
391 rate. During photocatalytic process, CuO_x based deposits were reduced to $\text{Cu}_2\text{O}/\text{Cu}^0$ and concurrently
392 a morphological evolution was also appreciated (Figure 9). Notably, deposits with less defined
393 morphology were observed in Cu(3%)/P25 sample after use, while larger CuO_x surface deposits were
394 observed in Cu(10%)/P25 sample. Previous reports provided evidence of Cu^{2+} reduction to Cu^+ ^[22, 36]
395 and to Cu^0 ^[41] under UVA irradiation.



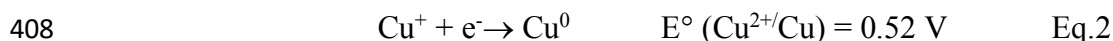
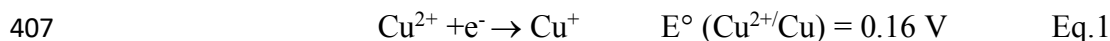


396

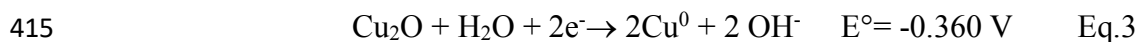
397 **Figure 9.** HR-TEM for Cu(3%)/P25 sample fresh (A) and after used (B) and for Cu(10%)/P25
 398 sample, before (C) and after used (D).

399

400 Experimental findings and in particular morphological evolution from HR-TEM analysis as well as
 401 Cu changes in copper surface availability after use (Table S5, Supplementary Information) suggested
 402 that CuO_x species undergo in situ dynamic nanostructuring during photocatalytic run. The process is
 403 driven by the dissolution-redeposition of CuO_x deposits on the TiO₂ surface under UV irradiation.<sup>[56-
 404 57]</sup> In more detail, CuO_x species must be involved in a dissolution process, leading to Cu²⁺ ions, that
 405 upon illumination are reduced to Cu₂O and then to Cu, by photo-generated electrons, according to
 406 Equations 1 and 2, both involving dissolved Cu ions:



409 In fact, electrochemical potentials of both half-reactions are higher than H⁺ species, supporting the
 410 hypothesis of Cu²⁺ and Cu⁺ preferential reduction by TiO₂ photogenerated electrons. The excess of
 411 electrons in the Cu deposits, accompanied by the consumption of photogenerated holes by methanol,
 412 allowed for the deposits to keep a metallic state throughout the reaction, as experimentally confirmed.
 413 Actually, negative electrochemical potential of solid state reduction further supports the hypothesis
 414 of reduction from solution (Equation 3).

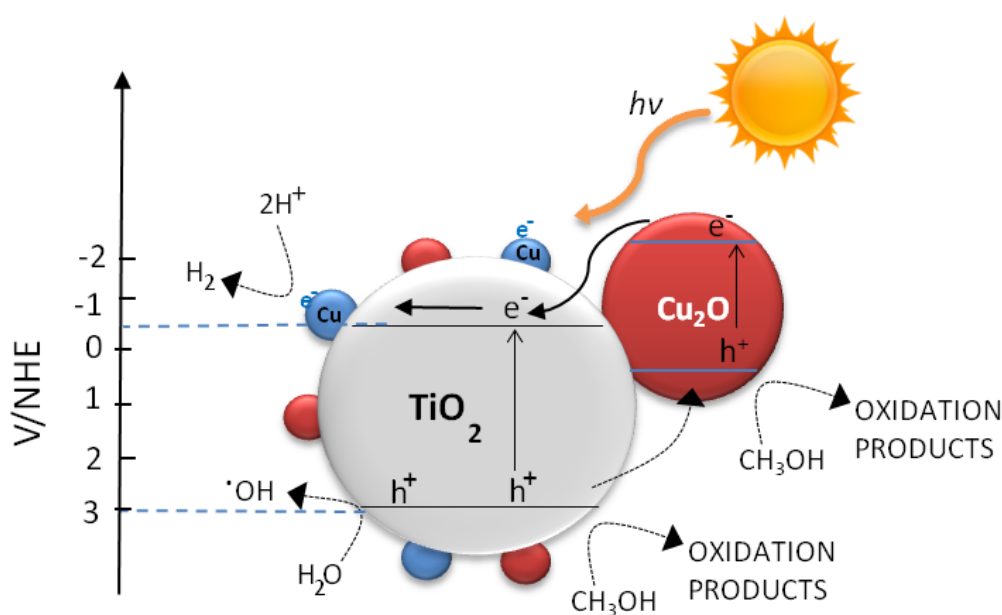


416 Indeed, Cu_2O reduction to metallic Cu was not revealed by previous studies on Cu impregnated
 417 TiO_2 ,^[22] however these differences should depend on the size of CuO_x deposits and their interaction
 418 with TiO_2 surface, strongly influencing their reducibility.

419 Actually, change in size and distribution of Cu species on the surface, as evidenced by HR-TEM,
 420 supports this mechanism.

421 Actually, island-like morphology of copper species on TiO_2 surface suggests deposition-reduction
 422 process occurred according to the Volmer-Weber mechanism^[58]. Notably, the lattice parameters of
 423 the substrate, significantly affect the sizes and oxidation level of Copper deposits. On this basis, as
 424 evidenced by experimental results, Cu and Cu_2O species must be preferentially deposited on TiO_2
 425 surface, due to their very good crystal lattice matching with P25 substrate ($a_{\text{Cu}} = 0,3615 \text{ nm}$, a_{TiO_2}
 426 $\text{anatase} = 0,378 \text{ nm}$; $a_{\text{Cu}_2\text{O}} = 4,27$, $a_{\text{TiO}_2 \text{ rutile}} = 0,459 \text{ nm}$). As a further support, electrochemical deposition
 427 on a semiconducting surface leads to coexistence of Cu and Cu_2O species on the surface .

428 Metallic Cu nanoparticles, should act as a co-catalyst for H_2 production, attracting photogenerated
 429 electrons from TiO_2 and promoting their transfer to the protons,^[27] according to the scheme in Figure
 430 10.



431

432 **Figure 10.** Proposed hydrogen photogeneration mechanism for Cu/ Cu_2O / TiO_2 system.

433

434 At the same time, upon illumination, Cu_2O should inject photoelectrons into TiO_2 conduction band
435 and hosting holes from TiO_2 valence band (Figure 10). Electrons injected into TiO_2 bands should be
436 involved in H^+ reduction, thus accounting for H_2 production since the beginning of the photocatalytic
437 run. The increased presence of holes in Cu_2O may limit further reduction of the Cu^+ to Cu^0 as well as
438 methanol oxidation, thus accounting for constant pH values during photo-reforming. Both processes
439 restrict electron/hole recombination phenomena and account for improved photocatalytic activity of
440 Cu doped P25.^[27]

441

442 Conclusions

443 Altogether, our photocatalytic tests and the in-depth investigation on impregnated Cu/P25 systems
444 elucidated the nature of copper species active in hydrogen production on Cu/P25 systems. Our
445 findings showed that:

- 446 1) Both CuO and Cu_2O nanostructures were obtained onto Cu/P25 by impregnation and further heat
447 treatment in nitrogen.
- 448 2) The sample allowing the highest H_2 production rates showed the highest fraction of finely
449 dispersed CuO nanostructures, that during the photocatalytic process, CuO species undergo an
450 in situ dynamic nanostructuring, leading to a significant change in both oxidation state and size
451 distribution. This evolution is probably based on a dissolution-redeposition process. In particular,
452 CuO species were involved in a dissolution process, followed by reduction of Cu^{2+} ions to Cu^+
453 and Cu^0 by photo-generated electrons.
- 454 3) Both Cu_2O and Cu^0 acted as co-catalysts for H_2 generation. Upon illumination, the former injected
455 photoelectrons into TiO_2 conduction band. The latter acted as a co-catalyst, hosting
456 photogenerated electrons from TiO_2 and mediating their transfer to the protons. Both processes

457 restricted electron/hole recombination phenomena and accounted for improved photocatalytic
458 activity of Cu doped P25.

459 The obtained findings clearly outline Cu/P25 catalysts as complex and dynamic systems. Their
460 evolution during photocatalytic process must be influenced by solution properties as well as by
461 preparation conditions of the catalyst itself, that markedly affect both size distribution and dispersion
462 of Cu species, and ultimately lead to different ratios between copper oxidation states on the catalyst
463 surface, thus affecting H₂ production rate.

464 The present work highlights that in situ catalysts transformation could improve their performance,
465 lying the basis to explore this strategy to optimize activity of other catalytic systems.

466

467

468 **Experimental Section**

469 *Materials*

470 Methanol (99.8% v/v), P25-TiO₂ (80:20 anatase:rutile), sodium nitrite (NaNO₂, purity ≥97.0%) used
471 as filter and cupric nitrite hydrate (Cu(NO₃)₂·3H₂O, purity 99.9%) were purchased from Sigma
472 Aldrich. Bi-distilled water was used for the preparation of the reacting mixtures.

473 *Cu/P25 material preparation*

474 Copper (0.5, 3, 6, 10 and 16 wt %) was loaded on P25-TiO₂ by impregnation method.^[23] For each Cu-
475 modified P25-TiO₂ sample (Cu/P25), a required amount of P25-TiO₂ was dispersed in Cu(NO₃)₂
476 aqueous solution. Excess water was evaporated to dryness with slow heating rate and constant
477 stirring. The samples were dried at 110 °C and then calcined under nitrogen atmosphere for 5h at
478 different temperatures ranging between 150 °C and 550 °C.

479 *Photocatalytic runs*

480 Photocatalytic runs were carried out in triplicate in an annular glass batch reactor (V=300 mL)
481 covered with a layer of aluminum foil. The reactants and nitrogen gas were fed to the reactor through

482 its top inlet hole, while collection of outflow liquid and gaseous samples was performed at the bottom
483 hole of the reactor at different reaction times. The reactor has been endowed with a high-pressure
484 mercury vapor lamp (input power: 125 W) manufactured by Helios Italquartz emitting in both
485 ultraviolet and visible range.

486 The lamp had ultraviolet emission peaks at 305, 313, and 366 nm corresponding to irradiances of
487 2.23×10^{-6} , 2.76×10^{-6} and 3.37×10^{-6} (E/s). The visible emission peaks at 405, 408, 436, and 546,
488 corresponded to irradiances of 6.18×10^{-7} , 1.41×10^{-7} , 1.03×10^{-6} , and 1.16×10^{-6} E/s, respectively. The
489 reactor was cooled at 25 °C during each run by means of a thermostatic bath (Falc GTR 90).

490 In order to evaluate the response of the photocatalytic system under visible light irradiation, during
491 the experimental runs water in the cooling jacket was replaced by 1M NaNO₂ solution absorbing
492 ultraviolet radiation, as reported elsewhere.^[40] The pH of the solution was monitored by means of an
493 Orion 420Ap pH-meter (Thermo).

494 In order to avoid the undesired reaction of dissolved oxygen with photogenerated electrons, before
495 starting the photocatalytic runs, a nitrogen stream was bubbled into the solution for 30 minutes for
496 removing atmospheric oxygen. Moreover, throughout the experiments, nitrogen was continuously fed
497 at a flow rate (Q_{N_2}) of 0.3 L/min to prevent any entrance of air into the reactor. For each run, fixed
498 amounts of photocatalysts and methanol (10% v/v) were added to 300 mL of aqueous solution; the
499 resulting suspension was sonicated and fed into the batch reactor under magnetic stirring. The liquid
500 samples, collected at different reaction times, were quickly filtered on regenerated cellulose filters
501 (pore diameter 0.20 μm, Scharlau) and the filtrate was used to measure dissolved copper and formic
502 acid concentrations. The gaseous samples were recovered from the reactor outlet in Tedlar gas
503 sampling bags and then used to evaluate hydrogen concentration.

504 Dissolved copper concentration was measured by means of a colorimetric method using an analytical
505 kit (Macherey–Nagel) based on oxalic acid bis-cyclohexylidene hydrazide (cuprizone). A UV/Vis
506 spectrometer (Cary 100 UV–Vis, Agilent) was employed for the measurements at a wavelength of
507 585 nm.

508 Hydrogen concentration was measured by a gas-chromatograph (Agilent 7820A) equipped with a
509 HP-PLOT Molesieve 5A column (Agilent) and a TCD detector using argon as carrier gas. During
510 the experiments, the radiation transmitted by the reactor was measured by means of a radiometer (not
511 shown in the figure) in the range 315-400 nm and 401-1100 nm.

512 *Physico-chemical characterization of the Cu/P25 nanomaterials*

513 A physico-chemical investigation on Cu/P25 nanomaterials was performed by using a combined
514 approach of different analytical techniques, such as High Resolution Transmission Electron
515 Microscope (HR-TEM, X-Ray Diffraction (XRD), Temperature-Programmed Reduction (TPR),
516 Raman, Electron Paramagnetic Resonance (EPR), and X-Ray Photoelectron Spectroscopy (XPS)
517 spectroscopies. Also, the specific surface area (S_{BET}) of catalysts was also determined through BET
518 porosimetry. Finally, H₂ Temperature Programmed Reduction (H₂-TPR) analysis was also
519 performed. The characterization was specifically focused on Cu(3%)/P25 and Cu(10%)/P25 catalysts
520 before and after their use in the photo-reforming process.

521 BET analysis allowed determining the specific surface area (S_{BET}), that was evaluated by generating
522 seven-point isotherms at 77 K for N₂ adsorption (Autosorb-1, Quantachrome) using the charred
523 sample capable of providing a specific surface area equal to 5 m² in the sample cell.

524 Raman spectra of the prepared catalysts were performed by using a confocal Raman Microscope
525 (Jasco, NRS-3100). Both the 514 nm line of an air-cooled Ar⁺ laser (Melles Griot, 35 LAP 431-220)
526 and the 647 nm line of a water-cooled Kr⁺ laser (Coherent Innova 302C) were used. The laser line
527 was injected into an integrated Olympus microscope and focused to a spot size of approximately 2
528 mm by using a 100× or 20× objective. A holographic notch filter was used to reject the excitation
529 laser line. Raman scattering was collected by using a Peltier-cooled 1024×128 pixel CCD photon
530 detector (Andor DU401BVI). For most systems, it took 60s to collect a complete data set. XRD
531 measurements were performed using a PANalytical diffractometer with a nickel filter and Cu K_α
532 radiation.

533 EPR experiments were carried out by means of X-band (9 GHz) Bruker Elexys E-500 spectrometer
534 (Bruker, Rheinstetten, Germany), equipped with a super-high sensitivity probe head. Solid samples
535 were transferred to flame-sealed glass capillaries which, in turn, were coaxially inserted in a standard
536 4 mm quartz sample tube. Measurements were performed at room temperature. The instrumental
537 settings were as follows: sweep width, 1500 G; resolution, 1024 points; modulation frequency, 100
538 kHz; modulation amplitude, 1.0 G. 16 scans were accumulated to improve the signal-to-noise ratio.
539 TPR measurements were carried out in a laboratory flow apparatus, using a 5% H₂/Ar ($Q=20\text{ cm}^3/$
540 min), with a heating rate of 10 °C/min up to 800 °C. The sample (60 mg) was loaded in a quartz
541 down-flow cell with a K thermocouple in close contact with the sample.
542 The nanoparticles morphology and crystallinity were investigated using a JEOL (JEM-2010F) high
543 resolution-transmittance electron microscope (HR-TEM) with the filed transmission of 200 kV. To
544 prepare the samples for HR-TEM, the catalysts were suspended in ethyl alcohol and sonicated for 45
545 min, then fixed on a Lacy Carbon grid (LC300, EMS) by the drop-casting method.
546 X-ray Photoelectron Spectroscopy (XPS) analysis was performed with a Versa Probe II Scanning
547 XPS Microprobe spectrometer (Physical Electronics GmbH). The measurements were done with a
548 monochromatized AlK α source (X-ray spot 100 μm), at a power of 24.4 W. Wide scans and detailed
549 spectra were acquired in Fixed Analyzer Transmission (FAT) mode with a pass energy of 117.40 eV
550 and 29.35 eV, respectively. An electron gun was used for charge compensation (1.0V 20.0 μA). All
551 binding energies were referenced to C1s at 284.8 \pm 0.1 eV for adventitious hydrocarbon. Data
552 processing were performed using MultiPak software v. 9.5.0.8.

553

554

555 **References**

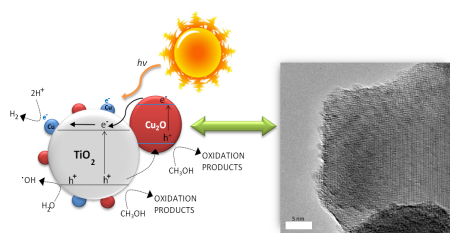
- 556 [1] G. Colon, *Appl. Catal. A* **2016**, *518*, 48-59.
557 [2] A.V. Puga, *Coord. Chem. Rev.* **2016**, *315*, 1-66.
558 [3] J. M. Valero, S. Obregón, G. Colón, *Appl. Catal. B Environmental* **2015**, *179*, 468-478.
559 [4] K. C. Christoforidis, P. Fornasiero, *ChemCatChem* **2017**, *9*, 1523-1544.

- 560 [5] K. C. Christoforidis, P. Fornasiero, *ChemCatChem* **2019**, *11*, 368-382.
- 561 [6] R. A. Rather, S. Singh, B. Pal, *J.Catal.* **2017**, *346*, 1-9.
- 562 [7] T. Montini, M. Monai, A. Beltram, I. Romero-Ocaña, P. Fornasiero, *Mater. Sci. Semicond.*
563 *Process* **2016**, *42*, 122-130.
- 564 [8] M. Hinojosa-Reyes, R. Camposeco-Solís, R. Zanella, V. Rodríguez González, *Chemosphere*,
565 **2017**, *184*, 992-1002.
- 566 [9] M. R. Pai, A. M. Banerjee, S. A. Rawool, A. Singhal, C. Nayak, S. H. Ehrman, A. K. Tripathi,
567 S. R. Bharadwaj, *Solar Energy Materials & Solar Cells* **2016**, *154*, 104-120.
- 568 [10] M. Karnahl, E. Mejía, N. Rockstroh, S. Tschierlei, S. P. Luo, K. Grabow, A. Kruth, V. Brüser,
569 H. Junge, S. Lochbrunner, M. Beller, *ChemCatChem* **2014**, *6*, 82-86.
- 570 [11] D. Barreca, P. Fornasiero, A. Gasparotto, V. Gombac, C. Maccato, T. Montini, E. Tondello,
571 *ChemSusChem* **2009**, *2*, 230-233.
- 572 [12] T. Montini, V. Gombac, L. Sordelli, J.J. Delgado, X. Chen, G. Adami, P. Fornasiero,
573 *ChemCatChem* **2011**, *3*, 574-577.
- 574 [13] V. Gombac, L. Sordelli, T. Montini, J. J. Delgado, A. Adamski, G. Adami, M. Cargnello, S.
575 Bernal, P. Fornasiero, *J. Phys. Chem. A* **2010**, *114*, 3916–3925.
- 576 [14] F. Teng, M. Chen, N. Li, X. Hua, K. Wang, T. Xu, *ChemCatChem* **2014**, *6*, 842-847.
- 577 [15] Z. Jiang, M. A. Isaacs, Z. W. Huang, W. Shangguan, Y. Deng, A. F. Lee, *ChemCatChem* **2017**,
578 *9*, 4268-4274.
- 579 [16] J. B. Priebe, J. Radnik, C. Kreyenschulte, A. J. J. Lennox, H. Junge, M. Beller, A. Brückner,
580 *ChemCatChem* **2017**, *9*, 1025-1031.
- 581 [17] D. Guerrero-Araque, P. Acevedo-Peña, D. Ramírez-Ortega, H. A. Calderon, R. Gomez, *Int. J.*
582 *Hydrogen Energ.* **2017**, *42*, 9744-9753.
- 583 [18] L. Clarizia, D. Spasiano, I. Di Somma, R. Marotta, R. Andreatti, D.D. Dionysiou, *Int. J.*
584 *Hydrogen Energ.* **2014**, *39*, 16812-16831.
- 585 [19] A.J.J. Lennox, P. Bartels, M.M. Pohl, H. Junge, M. Beller, *J. Catal.* **2016**, *340*, 177–183.
- 586 [20] Z. He, J. Fu, B. Cheng, J. Yu, S. Cao, *Appl. Catal. B* **2017**, *205*, 104-111.
- 587 [21] L.S. Yoong, F.K. Chong, Binay K. Dutta, *Energy* **2009**, *34*, 1652–1661.
- 588 [22] C. S. Chen, J. H. You, J. H. Lin, Y. Y. Chen, *Catalysis Communications* **2008**, *9*, 2381–2385.
- 589 [23] C. S. Chen, T. C. Chen, C. C. Chen, Y. T. Lai, J. H. You, T. M. Chou, C. H. Chen, J. F. Lee,
590 *Langmuir* **2012**, *28*, 9996–10006
- 591 [24] F. Boccuzzi, A. Chiorino, G. Martra, M. Gargano, N. Ravasio, B. Carrozzini, *J. Catal.* **1997**,
592 *165*, 129-139.
- 593 [25] F. Coloma, F. Marquez, C. H. Rochester, *Phys. Chem. Chem. Phys.* **2000**, *2*, 5320–5327.

- 594 [26] G. Wu, N. Guan, L. Li, *Catal. Sci. Technol.* **2011**, *1*, 601–608.
- 595 [27] K. Lalitha, G. Sadanandam, V. D. Kumari, M. Subrahmanyam, B. Sreedhar, N. Y. Hebalkar, *J.*
596 *Phys. Chem. C* **2010**, *114*, 22181–22189.
- 597 [28] M. Jung, J. N. Hart, J. Scott, Y. H. Ng, Y. Jiang, R. Amal, *Appl. Catal. A: General* **2016**, *521*,
598 190–201.
- 599 [29] A. Heciak, A. W. Morawski, B. Grzmil, S. Mozia, *Appl. Catal. B: Environmental* **2013**, *140–*
600 *141*, 108–114.
- 601 [30] A. J. Simamora, T. L. Hsiung, F. C. Chang, T. C. Yang, C. Y. Liao, H. P. Wang, *Int. J.*
602 *Hydrogen Energy* **2012**, *37*, 13855–13858.
- 603 [31] J. Yu, Y. Hai, M. Jaroniec, *J. Coll. Interf. Sci.* **2011**, *357*, 223–228.
- 604 [32] L. Li, L. Xu, W. Shi, J. Guan, *Int. J. Hydrogen Energy* **2013**, *38*, 816–822.
- 605 [33] J. Bandara, C.P.K. Udawatta, C.S.K. Rajapakse, *Photochem. & Photobiol. Sci.* **2005**, *4*, 857–
606 861.
- 607 [34] S. Xu, D. D. Sun, *Int. J. Hydrogen Energy* **2009**, *34*, 6096–6104.
- 608 [35] S. Xu, J. Ng, X. Zhang, H. Bai, D. D. Sun, *Int. J. Hydrogen Energy* **2010**, *35*, 5254–5261.
- 609 [36] P. Khemthong, P. Photai, N. Grisdanurak, *Int. J. Hydrogen Energy* **2013**, *38*, 15992–16001.
- 610 [37] A.L. Luna, M.A. Valenzuela, C. Colbeau-Justin, P. Vázquez, J.L. Rodriguez, J.R. Avendaño,
611 S. Alfaro, S. Tirado, A. Garduño, J.M. De la Rosa, *Appl. Catal. A: General* **2016**, *521*, 140–
612 148.
- 613 [38] Z. Xi, C. Li, L. Zhang, M. Xing, J. Zhang, *Int. J. Hydrogen Energy* **2014**, *39*, 6345–6353.
- 614 [39] J.M. Valero, S. Obregón, G. Colón, *ACS Catal.* **2014**, *4*, 3320–3329.
- 615 [40] M. Jung, J. Scott, Y.H. Ng, Y. Jiang, R. Amal, *Int. J. Hydrogen Energy* **2014**, *39*, 12499–12506.
- 616 [41] L. Clarizia, G. Vitiello, D. K. Pallotti, B. Silvestri, M. Nadagouda, S. Lettieri, G. Luciani, R.
617 Andreozzi, P. Maddalena, R. Marotta, *Int. J. Hydrogen Energy* **2017**, *42*, 28349–28362.
- 618 [42] D. M. Tobaldi, N. Rozman, M. Leoni, M. P. Seabra, A. S. Škapin, R. C. Pullar, J. A. Labrincha,
619 *J. Phys. Chem. C* **2015**, *119*, 23658.
- 620 [43] T.H. Fleisch, G. J. Mains, *Application of Surface Science* **1982**, *10*, 51–62.
- 621 [44] P. Cheng, W. Li, T. Zhou, Y. Jin, M. Gu, *J. Photochem. Photobiology A Chem.* **2004**, *168*, 97–
622 101.
- 623 [45] A. Compaan, H. Z. Cummins, *Phys. Rev. B* **1972**, *6*, 4753.
- 624 [46] H. F. Goldstein, Dai-sik Kim, Peter Y. Yu, L. C. Bourne, J-P. Chaminade, L. Nganga, *Phys.*
625 *Rev. B* **1990**, *41*, 7192.
- 626 [47] B. Choudhury, M. Dey, A. Choudhury, *Int. Nano Lett.* **2015**, *3*, 25.

- 627 [48] T. Oku, R. Motoyoshi, K. Fujimoto, T. Akiyama, B. Jeyadevan, J. Cuya, *J. Phys. Chem. Solids*
628 **2011**, 72, 1206-1211.
- 629 [49] N. Wongpisutpaisan, P. Charoonsuk, N. Vittayakorn, W. Pecharapa, *Energy Procedia* **2011**, 9,
630 404-409.
- 631 [50] J. F. Moulder, W. F. Stickle, P. E. Sobol and K. D. Bomben, *Handbook of X-Ray Photoelectron*
632 *Spectroscopy*, Physical Electronics Division, Perkin-Elmer Corp., Norwalk, **1995**.
- 633 [51] S. Esposito, M. Turco, G. Bagnasco, C. Cammarano, P. Pernice, A. Aronne, *Appl. Catal., A*
634 **2010**, 372, 48-57.
- 635 [52] S. Esposito, M. Turco, G. Bagnasco, C. Cammarano, P. Pernice, *Appl. Catal. A* **2011**, 403, 128-
636 135.
- 637 [53] M. Jung, H. Y. Ng, Y. Jiang, J. Scott, R. Amal, *Chemeca 2013: Challenging Tomorrow* **2013**,
638 214-217.
- 639 [54] G. Wu, N. Guan, L. Li, *Catal. Sci. & Technol.* **2011**, 1, 601-608.
- 640 [55] I. Rossetti, J. Lasso, E. Finocchio, G. Ramis, V. Nichele, M. Signoreto, A. Di Michele, *Appl.*
641 *Catal. A* **2014**, 477, 42-53.
- 642 [56] E. Aslan, I. H. Patir, M. Ersoz, *Chemistry-A European J.* **2015**, 21, 4585-4589.
- 643 [57] D.V. Shinde, Z. Dang, U. Petralanda, M. Palei, M. Wang, M. Prato, A. Cavalli, L. De Trizio
644 and L. Manna, *ACS Appl. Mater. Interfaces* **2018**, 10, 29583-29592.
- 645 [58] H. Bandarenka, S. L. Prischepa, R. Fittipaldi, A. Vecchione, P. Nenzi, M. Balucani and V.
646 Bondarenko, *Nanoscale Res. Lett.* , **2013**, 8, 85-93.

647

648 **Table of Contents**

649

650 CuO active species undergo in situ dynamic nanostructuring, through dissolution and photodeposition,
651 changing both oxidation state and size distribution

652